Assessing the optical configuration of a structured light scanner in metrological use

OPEN ACCESS
IOP Publishing
Measurement Science and Technology
Meas. Sci. Technol. **33** (2022) 085018 (16pp)
https://doi.org/10.1088/1361-6501/ac6e2f

Assessing the optical configuration of a structured light scanner in metrological use

Leonard Schild*, Fabian Sasse*, Jan-Philipp Kaiser and Gisela Lanza

wbk Institute of Production Science, Karlsruhe Institute of Technology (KIT), Kaiserstraße 12, 76131 Karlsruhe, Germany

E-mail: Leonard.Schild@kit.edu and Fabian.Sasse@kit.edu

Received 27 January 2022, revised 29 April 2022
Accepted for publication 9 May 2022
Published 23 May 2022

Abstract

Structured light scanners for three-dimensional surface acquisition (SL scanners) are increasingly used for dimensional metrology. The optical configuration of SL scanners (focal length and baseline distance) influences the triangulation process, on which the scanners' measurement principle relies. So far, only a limited number of studies has investigated the optical configuration's influence on the accuracy of a SL scanner. To close this gap, this work presents a design of experiment in which the optical configuration of a SL scanner is systematically varied and its influence on the accuracy evaluated. Further, tactile reference measurements allow to separate random from systematical errors, while a special test specimen is used in two different configurations to ensure general applicability of the findings. Thus, this work provides support when designing a SL scanner by highlighting which optical configuration maximizes accuracy.

Keywords: structured light, dimensional metrology, measurement uncertainty, design of experiments

(Some figures may appear in colour only in the online journal)

1. Introduction

1.1. Structured light sensors in metrological use

Optical systems with structured light projection for three-dimensional surface acquisition, called SL scanners in this paper, are now a widely used measurement technology. Such systems can be used for many applications and are becoming increasingly affordable [1]. This is due to technological advances regarding the projection methods, as well as the imaging and processing capabilities [2]. Advantages of optical 3D systems are their high acquisition speed and resolution, as well as being contactless [2, 3].

In a SL scanner, one or more camera systems and a light source with modulated light intensity are used to capture 3D surface information. While camera systems can only capture 2D information, the light source is used to project patterns of different light intensity. The camera systems are then able to detect the distortion of the pattern. The 3D surface information is calculated from this distortion [3]. Besides other types of analysis, dimensional measurements can be performed based on the surface information. The presented work deals with SL scanners used for dimensional measurements.

The whole workflow of a dimensional measurement with a SL scanner is depicted in figure 1. The workflow starts with specifying the measurement requirements (e.g. accuracy). In the next step, the system configuration is defined according

* Authors to whom any correspondence should be addressed.

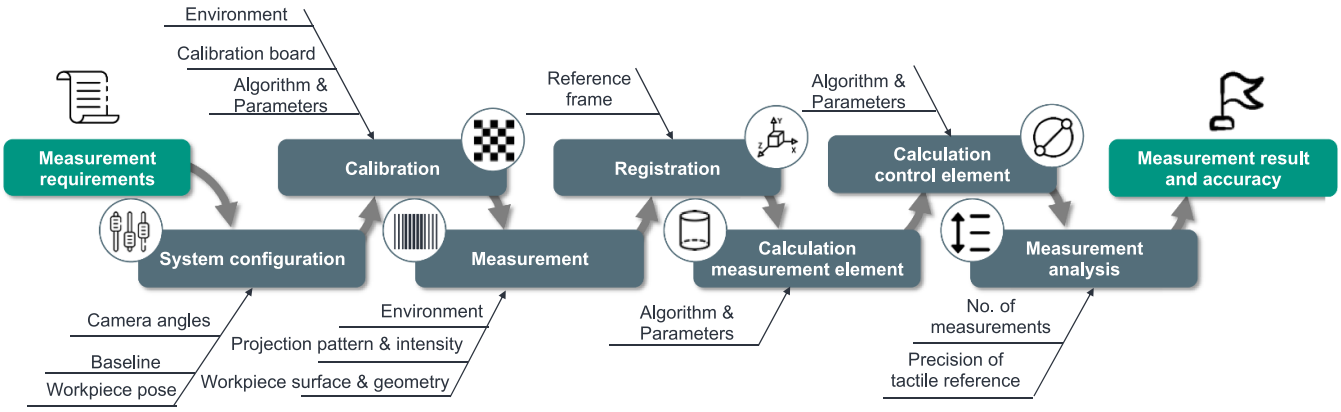

Figure 1. Standardized evaluation workflow with factors influencing the evaluation steps.

to the measurement requirements. This includes choosing an appropriate projector, camera sensors, lenses and the spatial arrangement of the components. Before an actual measurement is conducted, calibration is performed. In this step, camera parameters are determined with a calibration pattern. During the calibration process, the camera system parameters are obtained in respect to the physical properties of the calibration pattern. That is, the size of the calibration pattern allows traceability to the SI-unit of length (meter). After calibration, the image acquisition process takes place. During this step, patterns are projected on the specimen and images are acquired. After decoding the patterns in the images, triangulation is used to calculate a point cloud of the specimen. The point cloud is registered to a local specimen coordinate system by e.g. a best fit algorithm. Afterwards, points inside a region of interests are fitted to geometrical primitives such as planes or cylinders. Using one or combining several of these primitives, control elements like distances between planes or diameters of cylinders are calculated. The control elements represent properties of the specimen such as hole diameters or lengths.

1.2. Importance of system configuration of a SL scanner

During the second step of the measurement workflow, the system configuration, the measurement requirements are translated into technical specifications. Choosing the technical specifications carefully is important because they are the foundation for a good performance of the SL scanner. The technical specifications are typically divided into two groups: first, specifications regarding digitalization and, second, specifications regarding the optical configuration.

Digitalization specifications determine which sensor and projector are appropriate to fulfill a given task, i.e. scan features of a given workpiece in a certain environment. Besides costs, additional requirements as the required resolution, dynamic range, as well as noise characteristics of the sensor and projector, need to be considered.

The optical configuration is characterized by two major specifications: working distance and the given space the SL scanner may use. These two specifications lead to choosing an appropriate focal length of the lenses and a fitting baseline distance of the optical components. Figure 2 illustrates how different optical configurations allow for different working distances while requiring different amounts of space for a given object.

In contrast to the digitalization specifications, the optical configuration directly affects the triangulation process, which, in turn, determines the values of the dimensional measurements. Therefore, the optical configuration of a SL scanner is assumed to be of major importance for the accuracy of dimensional measurements performed with a SL scanner.

1.3. Research on the accuracy of SL scanners

The following overview presents publications dealing with the system configuration and the accuracy of SL scanners. The overview is structured according to the measurement process presented in figure 1.

Rachakonda *et al* [4] present a summary on different error sources in structured light scanners. While they cover different topics affecting accuracy, they stress that the SL scanner's construction is of major importance to the magnitude of the measurement errors. Besides the calibration or resolution, they state that the optical configuration can have a profound effect on measurement results.

Several authors deal with estimating the measurement uncertainty of a SL scanner as holistic as possible by deploying Monte Carlo (MC) based simulations. During these simulations, important factors influencing the measurement results are varied according to given probability distributions. Besides other factors, Sims-Waterhouse *et al* [5], Wu *et al* [6] and Liu and Li [7] investigate the baseline distance's and/or the focal length's influence on the measurement uncertainty by MC simulation. They all conclude that these factors related to the optical configuration have a strong impact on the measurement uncertainty. However, these papers do not focus on the design of SL scanners and thus do not provide explicit recommendations on how to choose an optical configuration that minimizes measurement uncertainty.

The optical configuration of a SL scanner has also been experimentally investigated. Sophian *et al* [8] evaluate the

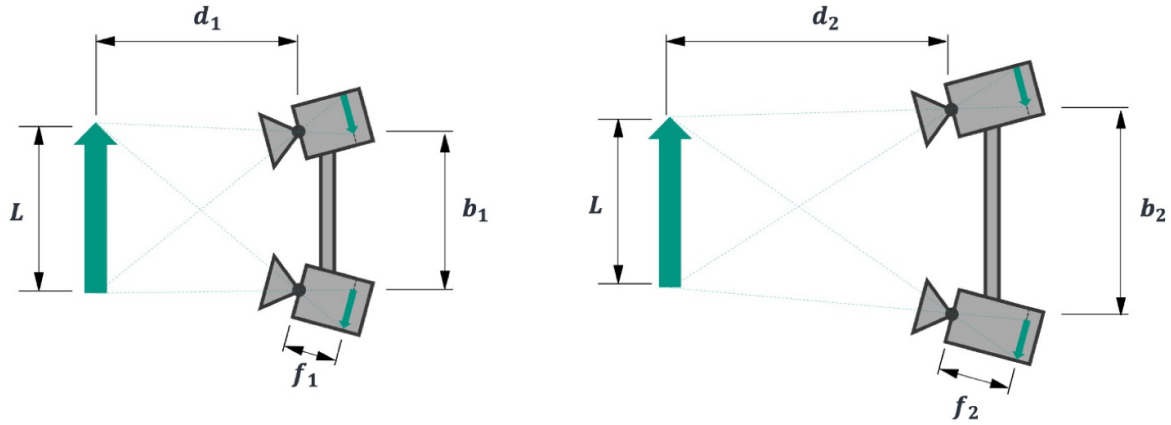

a) Configuration 1 b) Configuration 2

Figure 2. Comparison of two different optical configurations that enable a different working distance $d_2 > d_1$ for a given object (length L) by using different baseline distances ($b_2 > b_1$) and focal lengths ($f_2 > f_1$).

accuracy of an optical SL scanner when measuring a reference block of known length as a function of the distance of the block from the system. Setyawan *et al* [9] investigate the influence of the baseline distance between the two cameras. Only using a stereo vision system, the authors show, that the spatial arrangement influences finding corresponding points, which is also a relevant for SL scanners.

In contrast to the system configuration itself, the calibration is discussed by many authors. Subtopics are the investigation of different calibration patterns, optimization of the calibration model, the use of different calibration targets and the calibration procedure [10, 11]. An overview of commonly used calibration patterns is given by Guerra *et al* [12]. Typically, checkerboard patterns [12] or plates with circular patterns are used [10, 13–15]. In addition to the calibration targets, the models for computing the optimal calibration parameters are continuously improved [10, 14, 16].

The projection pattern plays a key role for the imaging process. Salvi *et al* [17] compare different projection strategies and discuss their advantages and limitations. Gupta *et al* [18] evaluate the influence of global illumination as a disturbance on the acquisition process and design an optimal combination of projection patterns to suppress these disturbances.

To evaluate the accuracy of an optical SL scanner many authors use a CAD model as a reference. For example, Li *et al* [19] use a GOM ATOS Triple Scan to measure a freeform surface and evaluate their acquisition result by registering the resulting point cloud to an existing CAD model using a best-fit algorithm. In contrast, Eiríksson *et al* [20] first measure the actual geometry of a standard calibration artefact according to VDI/VDE 2634 part 2 with a tactile coordinate measuring machine (CMM). The accuracy of the SL scanner is evaluated by comparing the measurement with tactile reference measurements. Spheres are fitted into the result of the tactile reference measurement as well as the measurement of the SL scanner and deviations of the control elements such as diameters are calculated. Guerra *et al* [12, 21, 22] use a similar approach to investigate how different materials and their optical properties influence the measurement accuracy of SL scanners. They use miniature step gauges which were measured by CMS to provide reference values. They conclude that the material can induce systematic errors for bi-directional features. Catalucci *et al* [23] measure additively manufactured freeform parts with a photogrammetry system and a SL scanner. Besides covering topics such as coverage and point density, they deploy CMM for reference measurements. Based on the CMM-provided reference values, they highlight how different types of measurement features induce systematic errors of varying magnitude.

CMM reference measurements have also been used for calibrating reference standards for acceptance testing. While the above-mentioned guidelines VDI/VDE 2634 parts 2 and 3 are most common, Guidi *et al* [24] and Iuliano *et al* [25] work on reference standards which are closer to representing actual industrial workpieces than the sphere standard from VDI/VDI 2634. More recent work by Ghandali *et al* [26] and Martínez-Pellitero *et al* [27] focus on simpler geometries to investigate effects related to the positioning of the SL scanner relative to the investigated object. While it is used for these SL scanner applications, deploying tactile reference measurements is even more common with other measurement techniques deploying image processing, like industrial computed tomography (CT) Müller *et al* [28].

In conclusion, this overview highlights two points. First, the influence of the optical configuration (focal length and baseline distance) on the measurement system's accuracy has not been systematically investigated, yet, although its importance for the accuracy of a SL scanner has been acknowledged by several authors. Second, while deploying tactile reference measurements allows to provide reference measurements and thus calculating systematic errors, most SL scanner-related work does not provide in-depth detail on how comparability of these two techniques is established. Without well-adapted reference measurements, it is impossible to assess the influence of the optical configuration on the accuracy of a SL scanner,

though. Therefore, these two research topics will be addressed in this work.

2. Procedure for assessing the optical configuration of a SL scanner

In this section, a general procedure is presented to assess the influence of the optical configuration of a SL scanner on its accuracy for different measurement tasks. The procedure consists of three parts. First, a modular SL scanner is described. Second, a convertible test specimen is presented. Third, the SL scanner and specimen are used to conduct a design of experiments (DoE). In the DoE, tactile reference measurements are used to evaluate the accuracy of the SL scanner. Experimental results of the DoE are presented in section 3.

2.1. Modular SL scanner

To study the influence of the optical configuration of a SL scanner on its accuracy, a modular SL scanner is used. By using different lenses and baseline distances, it is possible to realize different working distances and levels of packaging compactness with the modular SL scanner.

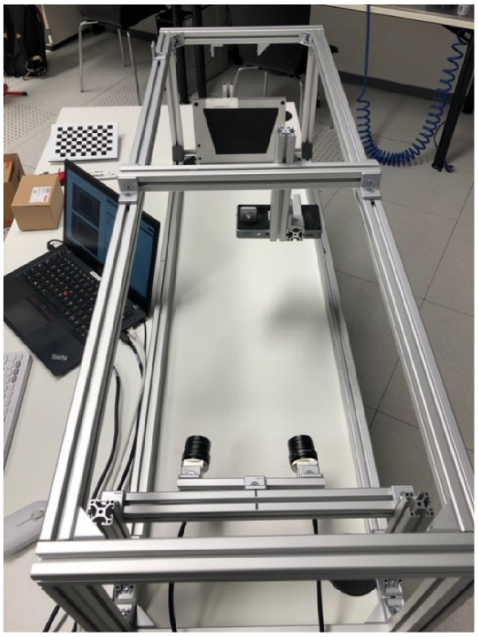

Figure 3. Test rig including the two cameras, the projector as well as the calibration target in the background.

2.1.1. SL scanner components. The modular SL scanner is depicted in figure 3. It consists of a frame made from aluminum profiles. Besides the test specimen, two cameras are mounted on the frame as well as a projector. Typical specimens measure a base size of about 200 × 200 mm. The frame allows working distances of up to 1000 mm and baseline distances of up to 400 mm. Image acquisition and processing is conducted with an evaluation PC running MATLAB 2020b from The MathWorks, Inc. (USA).

The structured light system uses a stereo setup in order to allow an easy calibration workflow. By using a stereo camera setup instead of a camera–projector combination, the stereo camera calibration may be conducted by using MATLAB's camera calibration tools.

Suitable cameras were chosen based on their resolution. For general use in production metrology, the cameras' resolution must allow to detect production deviations of an investigated specimen which are relevant compared to the specimen's tolerances. In case of this paper, test specimens instead of actual industrial workpieces were used, though. Therefore, the authors chose that the system should be able to detect deviations of about 0.1 mm. This value stems from the authors' experience in the field of automotive body in white production and battery cell assembly. To derive the actual resolution requirements, machine vision systems' capability of subpixel detection precision and the above mentioned 0.1 mm tolerance were together considered. Combining these, the authors decided that 1 pixel of the camera image should equal about 0.1 mm. Taking into account that the investigated specimens measure about 200 × 150 mm (see section 2.2.1 for more details), a camera resolution of about 2000 × 1500 pixels was found to be sufficient. Based on these requirements, cameras of type acA1920-40um by Basler AG (Germany) were chosen. These cameras feature the Sony IMX IMX249 sensor with a resolution of 1936 × 1216 pixels. Besides fulfilling the resolution requirements, these sensors features large diodes which give the cameras low image noise and high dynamic range (73.5 dB). Adding to this benefit, the cameras feature C-mount, which allows many different lenses to be used, and Basler provides software fully compatible to MATLAB.

To enable the implementation of robust decoding algorithms for the projected pattern, a common line pattern with $n_\mathrm{I} = 8$ images and a maximum of $n_\mathrm{l,max} = 2^{n_\mathrm{I}} = 128$ lines was chosen to be appropriate. In respect to costs and general availability, a projector with 1080p resolution was found to be sufficient to project such a pattern. A projector of make DLP LED Projektor COCAR C800S by Cocar (China) was therefore used.

Lenses with 16 and 25 mm focal length were used. They allow working distances of 400 and 700 mm, respectively. The lenses are of types LM16HC and LM25HC by KOWA Ltd (Japan).

A checkerboard target was custom-printed using UV-LED direct printing and is used to perform calibrations. The checkerboard measures 200 × 150 mm with squares of 15 mm size. To achieve good reproducibility for the calibration process, a 3D printed clamping is used. It allows the calibration target to be repeatably set to specific poses.

The cameras, lenses, projector, and the rest of the hardware are of common quality and may be substituted by other models with similar specifications. Using different focal lengths and baseline distances, is possible, as well. Using widely available hard- and software allows teaching facilities, like universities, to use a similar setup, e.g. for teaching or laboratory work. Furthermore, the code for using the system is available as git repository.

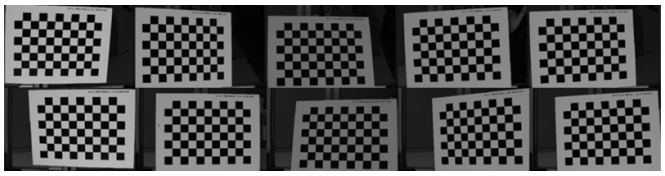

Figure 4. Exemplary images used for the calibration of the stereo camera system (top images belong to camera 1 and lower images belong to camera 2).

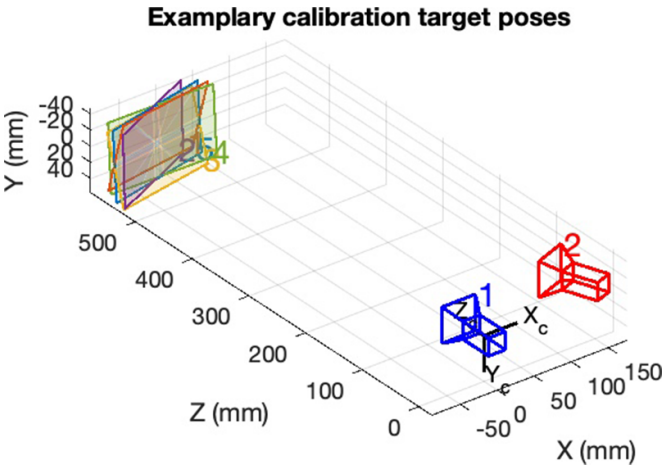

Figure 5. Exemplary visualization of the checkerboard's poses relative to the stereo cameras for the images of figure 4.

2.1.2. Image acquisition and processing. The image acquisition and processing were carried out with MATLAB toolboxes of the same names in versions 6.3 and 11.2, respectively. The image acquisition and processing steps are described in the following.

Before actual image acquisition, the camera system needs to be calibrated. Five images of the calibration pattern in pre-defined poses are captured. Exemplary images are shown in figure 4. Using MATLAB's calibration functions, which are based on the approaches by Zhang and Huang [29] and Heikkilae and Silven [30], a stereo camera object is created that includes the stereo camera parameters. Figure 5 shows the poses of the cameras relative to each other and to the checkerboard. The figures illustrate that, by using a checkerboard of the given size and the five pre-defined poses, it is possible to cover most of the volume in which measurements with the SL scanner are to be conducted.

For the actual image acquisition process, line patterns are projected onto the object scene. To do so, figures of the respective line patterns are created with MATLAB. These are opened in full screen mode on the virtual screen that belongs to the projector. This workflow eliminates the need for any further software. An image of each pattern is captured. All acquired images are stored in a 4D matrix (first dimension: y coordinates of image, second dimension: x coordinates of image, third dimension: image number, fourth dimension: camera of stereo setup).

Before decoding the pattern, the line pattern images are binarized using a local threshold according to Steger *et al* [31].

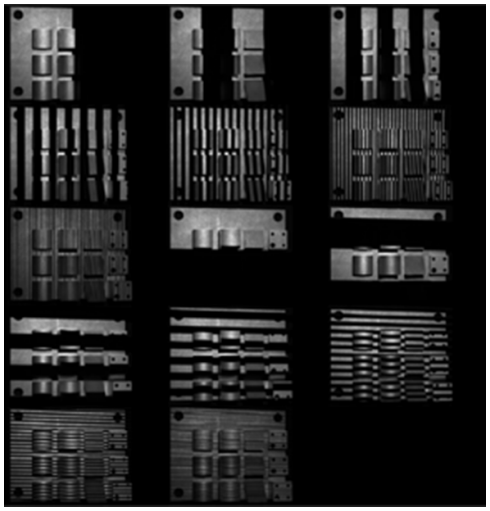

Figure 6. Images from one camera containing all patterns.

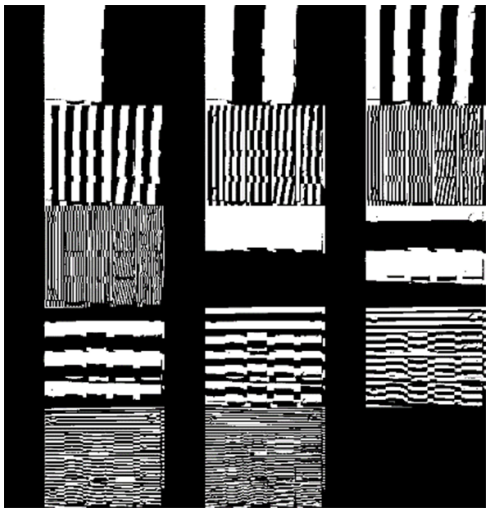

Figure 7. Binarized images from one camera of all patterns.

Figure 6 shows captured images and figure 7 their binarized versions.

To decode the pattern, the images of vertical and horizontal lines are decoded separately, first. Starting with the image with the least lines, the n_l binarized images of vertical lines $I_{\mathrm{bin,v,c}}$ and horizontal lines $I_{\mathrm{bin,h,c}}$ captured by camera c are weighted by factors w and overlayed to calculate the decoded images $I_{\mathrm{d,v,c}}$ and $I_{\mathrm{d,h,c}}$.

$$I_{\mathrm{d,v,c}} = \sum_{i=1}^{n_\mathrm{l}} w_i \, I_{\mathrm{bin,v,c},i}$$

$$I_{\mathrm{d,h,c}} = \sum_{i=1}^{n_\mathrm{l}} w_i \, I_{\mathrm{bin,h,c},i}.$$

The weight w_i of image I_i is determined according to the number of the ith image and the total number of images n_l.

$$w_i = 2^{n_\mathrm{l}-i}.$$

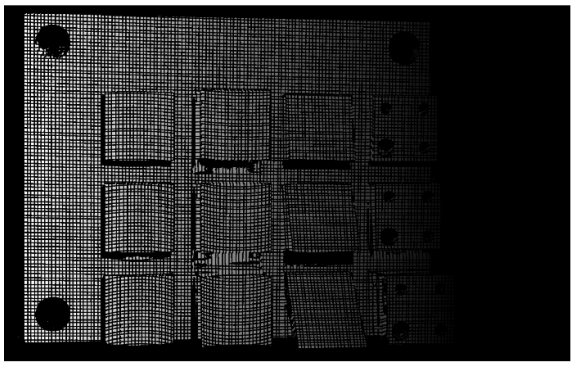

a) Image from camera 1

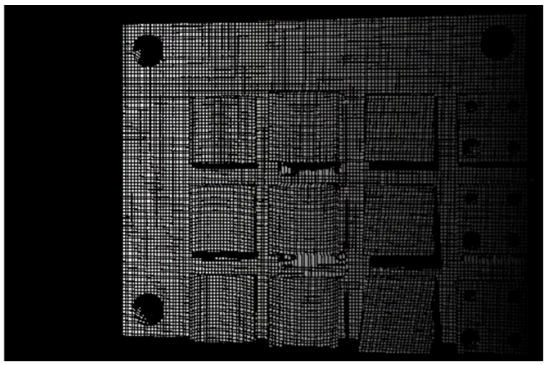

b) Image from camera 2

Figure 8. Decoded binarized images after applying binary mask with grey values translating to indices.

The decoded image $I_{\mathrm{d,c}}$ of camera c is calculated by adding the decoded image of vertical lines $I_{\mathrm{d,v,c}}$ to the one of the horizontal lines $I_{\mathrm{d,h,c}}$. To ensure unambiguous identification of a given column and row of the pattern, i.e. an index from the pattern, the image of the vertical lines $I_{\mathrm{d,v,c}}$ is multiplied by the number of columns $n_{\mathrm{col}} = 2^{n_{\mathrm{l}}}$. On a note, the number of rows and columns are equal in this work.

$$I_{\mathrm{d,c}} = n_{\mathrm{col}} I_{\mathrm{d,v,c}} + I_{\mathrm{d,h,c}}.$$

In the decoded image I_{d}, grey values respond to indices in the pattern. Morphological erosion is then used on the binarized version of the images of the finest stripes to create a binary mask. The binary mask is applied to the decoded image and defines which pixels are used for the following triangulation process. Figure 8 shows images of the decoded line pattern for both cameras after a binary mask was applied.

In the next step, corresponding points are detected in both images and then triangulated. To identify corresponding points, the grey values of both images are analyzed. First, the x and y values of the centroids of areas with similar grey values are calculated for both images. Second, the centroid values are stored in a $n_{\mathrm{ind}}x2$ matrix M in which row i represents index i from the n_{ind} indices of the line pattern, the first column the x values and the second column the y values of the centroids. Third, both images' centroid matrices M_1 and M_2 are used for triangulation. As the row numbers translates to the index number of the line pattern, centroid values from row i of centroid matrix of the first camera $M_{1,i} = (x_{1,i}, y_{1,i})$ correspond to the centroid values from the same row of centroid matrix of the second camera $M_{2,i} = (x_{2,i}, y_{2,i})$. To obtain a world point $p_{w,i} = (x_{w,i}, y_{w,i}, z_{w,i})$, corresponding points $(x_{1,i}, y_{1,i})$ and $(x_{2,i}, y_{2,i})$ are triangulated by deploying the camera parameters cp and the MATLAB function triangulate.

$$(x_{w,i}, y_{w,i}, z_{w,i}) = \mathrm{triangulate}\left(\mathrm{cp}, (x_{1,i}, y_{1,i}), (x_{2,i}, y_{2,i})\right).$$

Triangulating all n_{ind} corresponding points gives a list p_{w} of world points, which forms a point cloud of the object scene, as shown in figure 9.

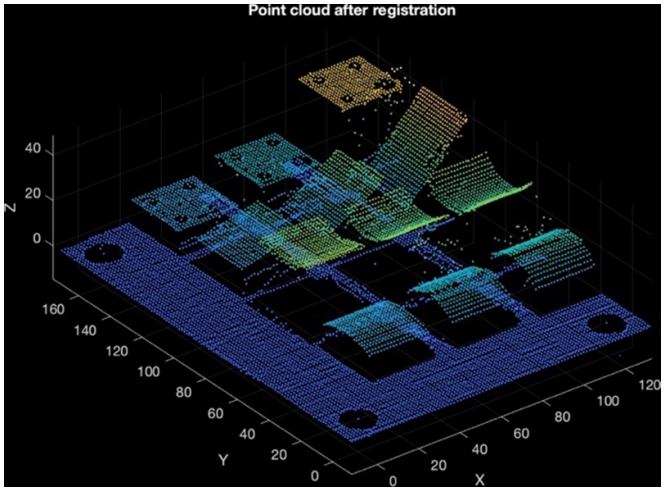

Figure 9. Point cloud calculated from images.

2.1.3. Metrological processing. To achieve comparability between tactile reference measurements and optical measurements, measurement and control features must be evaluated in the same way for the tactile CMM and the SL system. To ensure this comparability, the metrological processing of the point cloud is modelled in MATLAB to precisely equal the CMM software's processcing.

During the metrological processing, so-called measurement features and control features are calculated. Measurement features describe the geometric properties of specific areas of the specimen in an abstract way by means of a mathematical model. For example, a flat part of the workpiece could be described by a plane. The four plane parameters are calculated by first choosing those points of the point cloud that represent the given area and then deploying a suitable fitting algorithm. The measurement features used in this paper are given in table 1. While measurement features represent the geometric properties of the specimen, they do not necessarily allow to derive measurement results that can be compared to the nominal sizes or to be used to determine the accuracy. For example, to calculate the distance between two flat parts of a specimen, one plane is not sufficient. Further, some measurement features allow to derive different measurement results,

Table 1. Measurement features used in this paper.

Name	Points used	Algorithm
Plane	All points of point cloud inside ROI	MATLAB implementation using RANSAC
Cylinder	All points of point cloud inside ROI	Nonlinear optimization according to SRC
Circle	All points identified by Hough transformation in one 2D image	MATLAB implementation using Pratt's method
Point	Center of circle	See above

e.g. a circle fitted to a hole allows to deduct the circle centers' x, y and z coordinates as well as its diameter. For this reason, so-called control features are distinguished from the measurement features. Control features are calculated by processing one or more measurement features. Table 2 provides explanations on how the measurement features used in this paper are processed to calculate the control features. It is typical of commercial measurement software to differentiate between measurement and control features and helps to achieve repeatable as well as unambiguous measurement results. The complete evaluation process consists of the following steps:

(a) Determine characteristic measurement features for registration (e.g. the centers of easy to detect circles)
(b) Perform registration of point cloud
(c) Divide point cloud in different regions of interests (ROI)
(d) Fit measurement elements to specified ROIs
(e) Calculate control elements.

2.2. Convertible test specimen

A test specimen with variable geometry was designed to investigate the influence of the optical configuration on the accuracy of a SL scanner. By using two different geometric configurations of the specimen, it was possible to separate the influence of workpiece geometry from the influence of the optical configuration. First in this section, the basic design of the convertible test specimen is presented. Afterwards, two configurations are shown, which are used in the DoE in section 2.3.

2.2.1. Basic design of convertible test specimen. The convertible specimen's base plate is shown in figure 10. It is made from aluminum, has a size of 145 × 185 mm and a thickness of 14 mm. Holes with a diameter of 15 mm are drilled in three corners. These are used to register the point cloud. Four threads are embedded on the underside of the component so that it can be fixed to the aluminum profiles of the test rig.

All surfaces of the test specimen have been sandblasted to reduce reflections. Holes have not been deburred to enable unambiguous edge detection during image processing. To simplify image processing, black cardboard was applied to the bottom of the holes.

Twelve places are provided on the base plate to fit different elements. By using different geometric elements, the test specimen's shape may be altered. In total, four element types are available: flat planes with holes, sloped planes, concave surfaces and convex surfaces. All elements are designed to ensure that it is possible to measure them with a tactile CMM.

An element is first centered in the middle with a dowel pin. Then the alignment is determined; each element can be mounted in any direction. The element is then fixed from below with a screw.

All parts of the test specimen were machined by means of milling. Standard tolerances according to ISO 2768 were used for manufacturing the parts. The parts were afterwards measured using a tactile CMM. During these measurements, the test specimens' dimensions were accurately determined and used for calculating the systematic errors (see section 2.3.2 for more details). Further, form errors (planarity and cylinder form) were checked for all measurement features (more details on the test specimen's measurement features in the next

Table 2. Control features calculated in this paper.

Name	Processed measurement features	Processing steps
Distance	Two planes	• Center point (mean of all points) of first plane and normal vector of second plane are used to calculate the penetration point of second plane. • Distance is measured by Euclidian distance between center point and penetration point.
Angle	Two planes	Angle is represented by angle enclosed by the normal vectors of two planes
Diameter	One cylinder or one circle	• For cylinders the diameter of fitted measurement feature is evaluated. • For circles the diameter, which is evaluated in the 2D image of camera 1, is transformed to world coordinate system by using the z-distance from the point of the circle to the projection center as well as the focal length by $\left(d_{\text{world}} = \frac{z}{f} d_{\text{image}}\right)$.
Position	One point	Position in registration coordinate system is evaluated.

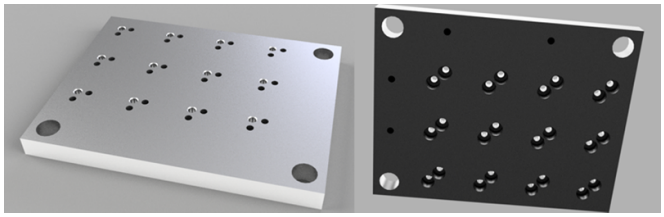

Figure 10. Base plate of the reference component (left: top view, right: bottom view).

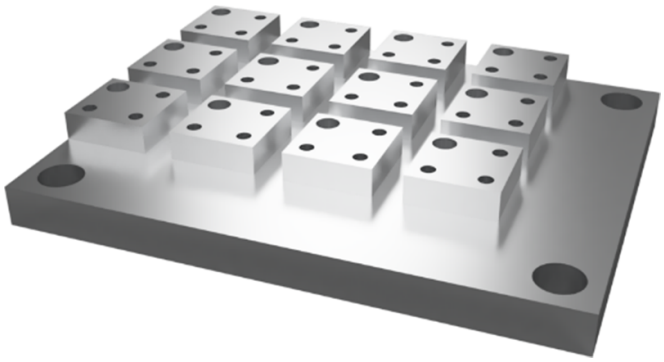

Figure 11. Flat configuration of the test specimen consisting of the base plate and 12 identical elements.

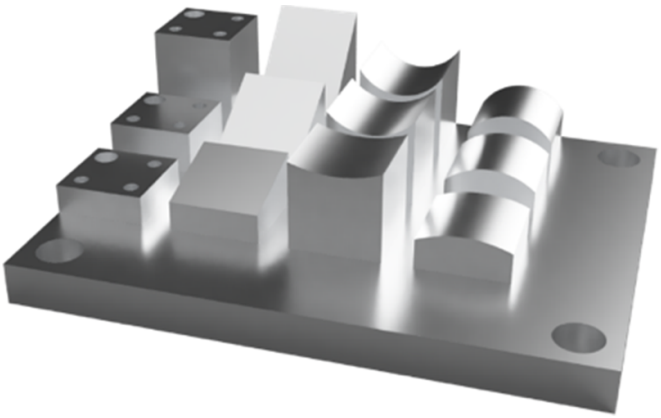

Figure 12. Topographical configuration of the test specimen consisting of the base plate and various elements.

subsection). While an average form error of 0.023 mm was measured, no feature's form error was found to be bigger than 0.049 mm. These values were accepted as being sufficiently low to allow for unambiguous registration and precise measurements of the measurement features.

2.2.2. Test specimen configurations. Two configurations are used during the DoE presented in the next section. A so-called 'flat' configuration and a 'topographical' configuration. The flat configuration only consists of elements in one plane while the topographical configuration uses 3D elements.

Using these two different configurations allows to differentiate the influence of the SL scanner's optical configuration on the measurements' accuracy from the influence of the shape of different geometric elements on the accuracy. The flat configuration only consists of elements in one plane and, therefore, mainly shows the influence of the optical configuration on the accuracy. Measurements of the topographical configuration are influenced by the geometric shape of the features as well as by the optical configuration. Comparing results from the topographical configuration's measurements to those of the flat configuration allows to distinguish the specimen shape's influence on the measurements from the influence of the optical configuration.

The flat configuration is shown in figure 11. It consists of 12 similar elements. All are of square layout and feature four holes each (total 48 holes). The elements have a base area of 30 × 30 mm and a height of 5 mm. One hole is bigger than the others to allow unambiguous identification of the different features. The diameters measure 5 and 8 mm respectively. The control features are the x and y coordinates of the centres of the holes as well as the diameters of the holes.

The topographical configuration is shown in figure 12. Twelve different geometrical elements with an identical base area of 30 × 30 mm are arranged on the base. Four different types of elements are used: flats, slants, concave surfaces and convex surfaces. Elements of type flat resemble those previously used for the flat configuration. Besides the holes' x coordinates, y coordinates and diameters, the distance between the baseplate and the surface of the elements is measured. In case of the slants, their angle relative to the baseplate is determined. The convex and concave elements' measurement features are cylinders and the cylinders' diameters are used as control features.

Table 3. Control features of the geometric elements of the test specimen in topographical configuration.

Geometric element	Control features	Characteristics
Holes on 35 mm flat	x, y coordinates and diameter	Different
Holes on 15 mm flat	x, y coordinates and diameter	Different
Holes on 5 mm flat	x, y coordinates and diameter	Different
Surface on 35 mm flat	z coordinate	35 mm
Surface on 15 mm flat	z coordinate	15 mm
Surface on 5 mm flat	z coordinate	5 mm
Slanted surface	Angle	Angle 45°
Slanted surface	Angle	Angle 30°
Slanted surface	Angle	Angle 15°
Concave surface	Diameter	Diameter 35 mm
Concave surface	Diameter	Diameter 40 mm
Concave surface	Diameter	Diameter 80 mm
Convex surface	Diameter	Diameter 35 mm
Convex surface	Diameter	Diameter 45 mm
Convex surface	Diameter	Diameter 76 mm

The features' dimensions were chosen to resemble typical industrial workpieces of similar size, e.g. automotive parts. Due to the modular structure of the test specimen, it is easily possible to change dimensions for the geometric elements to more closely resembled those of a specific set of industrial workpieces, though. All elements' measurement features and control features are summarized in table 3.

2.3. Design of experiments for assessing the optical configuration

The previously described modular SL scanner and convertible test specimen are used in a DoE. The DoE aims at assessing the influence of the optical configuration on the accuracy of the SL scanner. First, the test design is presented. Afterwards, it is described how the accuracy, which is used as response variable of the DoE, is evaluated.

Table 4. List of experiments.

Experiment	Test specimen configuration	Optical configuration	Focal length	Baseline distance
1	1 (flat)	1	16 mm	90
2		2		150
3		3	25 mm	90
4		4		150
5	2 (topographic)	1	16 mm	90
6		2		150
7		3	25 mm	90
8		4		150

2.3.1. Conducting the design of experiments. In the DoE, the baseline distance between the cameras, the focal length of the lenses and the geometric configuration of the test specimen are factors. These three factors are varied in two levels. In total, the DoE consists of eight experiments. They are listed in table 4.

To evaluate the DoE, the accuracy is quantified by the expanded measurement uncertainty U and the systematic error b as described in the next subsection. To separate random from systematic effects, each experiment is conducted multiple times. To do so, the image acquisition process as well as the camera calibration process are repeated five times. When repeating the image acquisition process, not only taking the images is repeated, but instead the whole measurement procedure is repeated, which includes disassembling and remounting the test specimen as well as the cameras on the test rig. Further, both processes are repeated independently from each other. First the calibration process is repeated $n_{\mathrm{cal}} = 5$ times and only then the image acquisition is repeated $n_{\mathrm{img}} = 5$ times. This allows to evaluate the same repetition of the image acquisition process with different calibrations. Thus, it is possible to differentiate between the influence of repeating the calibration process and repeating the image acquisition process.

Further important influence factors are treated as control variables, which are held constant. They include temperature and ambient light. These are held constant by performing the measurements in a measurement room with climate control with the lights switched off.

2.3.2. Evaluating the measurement accuracy. To quantify the accuracy, the expanded measurement uncertainty U and the systematic error b are determined by using a calibrated workpiece as described in DIN EN ISO 15530-3.

In a first step of adopting the DIN ISO 15530-3 approach, the test specimen is calibrated, i.e. reference measurements are conducted. For this purpose, a tactile CMM is deployed in this paper. A CMM is chosen because CMMs are known to allow for measurements of low measurement uncertainty. The measurement process of the SL scanner is designed to match the one of the tactile CMM as closely as possible to allow the DIN ISO 15530-3 approach to be adopted. Both measurement processes are compared in table 5.

To calibrate the test specimen, each configuration of the test specimen is measured five times with a tactile coordinate machine of type O-INSPECT 322 (probing error 8 µm) by Zeiss IMT GmbH (Germany) using the software Zeiss Calypso 2018 also by Zeiss IMT GmbH. The mean values of all measurement repetitions are used as calibration values of the different features.

Table 5. Description of steps of coordinate measuring process comparing tactile CMM to SL scanner.

No.	Description	Tactile	SL scanner
1	Measure coordinates of points on surface of test object with reference to CMS coordinate system	Tactile probing of surface	Triangulation of matched points
2	Fit measurement features (e.g. cylinder) to the points	Same: dependent on processing program used	
3	Calculate control features (e.g. diameter) by processing measurement features	Same: dependent on processing program used	

In a next step of adopting the DIN EN ISO 15530-3 approach, the expanded measurement uncertainty U and the systematic error b are calculated for a measurand y, i.e. a particular control feature, to give the complete measurement result Y.

$$Y = y \pm U - b.$$

The systematic error b is derived by subtracting the tactile calibration measurement result y_{cal} from the mean of repeated SL scanner measurement values $\bar{y}$.

$$b = \bar{y} - y_{\mathrm{cal}}.$$

The expanded measurement uncertainty U consists of four standard uncertainties u which are combined in a root sum of squares and an expansion factor k. The expansion factor k ensures that the expanded measurement uncertainty U covers most measurement values typically encountered during repeated measurements. Here, a value of $k = 2$ is chosen which accounts for about 95% of measurements of a normally distributed measurement process.

$$U = k\sqrt{u_{\mathrm{cal}}^2 + u_{\mathrm{p}}^2 + u_{\mathrm{b}}^2 + u_{\mathrm{w}}^2}.$$

In the formula, u_{cal} is the standard uncertainty of the calibration, u_{p} the standard uncertatinty of the measurement process, u_{b} the standard uncertainty of correcting the systematic error and u_{w} the standard uncertainty of material and production variation. Of these uncertainty contributions, the standard uncertainty of the measurement process u_{p} assesses random errors resulting from the measurement process itself, like image noise or measuring positions varying during process repetitions. In this work, u_{p} is calculated according to the following formula to consider all n_{cal} repetitions of the calibrations and all n_{img} repetitions of the image acquisition process. In the formula, $y_{i,j}$ relates to the measurement values obtained from the ith repetition of the image acquisition process and the jth repetition of the calibration process.

$$u_{\mathrm{p}} = \sqrt{\frac{1}{n-1}\sum_{i=1}^{n_{\mathrm{img}}}\sum_{j=1}^{n_{\mathrm{cal}}}(y_{i,j}-\bar{y})^2}.$$

For this work, it is assumed that the uncertainty of the tactile calibration is much smaller than the uncertainty of the optical measurement process $u_{\mathrm{cal}} \ll u_{\mathrm{p}}$. Additionally, by measuring in the same measurement room with controlled temperature and only using the same specimen, the standard uncertainties u_{b} and u_{w} may be ignored as well, as they are only dependent on the temperature and a variation of the specimen, respectively. These assumptions reduce the contributors to the expanded measurement uncertainty U to the expansion factor k and the standard deviation of the measurement process u_{p}.

$$U \approx k u_{\mathrm{p}}.$$

In a final step of adopting the DIN EN ISO 15530-3 approach, the influence of repeating the camera calibration process on the measurement uncertainty is evaluated separately from the influence of repeating the image acquisition process. For this evaluation, two variations of the standard uncertainty of the measurement process are calculated.

The standard deviation of the calibration process $u_{\mathrm{p,\,cal}}$ is determined by first only considering repetitions of the calibration process and then calculating a mean value for all repetitions of the image acquisition process.

$$u_{\mathrm{p,\,cal}} = \left(\sum_{i=1}^{n_{\mathrm{img}}}\sqrt{\frac{1}{n-1}\sum_{j=1}^{n_{\mathrm{cal}}}(y_{i,j}-\bar{y})^2}\right) \Big/ n_{\mathrm{img}}.$$

The standard deviation of the image acquisition process $u_{\mathrm{p,\,img}}$ is determined conversely, i.e. by first only considering repetitions of the image acquisition process and then calculating a mean value for all repetitions of the calibration process.

$$u_{\mathrm{p,\,img}} = \left(\sum_{j=1}^{n_{\mathrm{cal}}}\sqrt{\frac{1}{n-1}\sum_{i=1}^{n_{\mathrm{img}}}(y_{i,j}-\bar{y})^2}\right) \Big/ n_{\mathrm{cal}}.$$

In summary, the systematic error b and the expanded measurement uncertainty U quantify the accuracy of the SL scanner to evaluate the DoE. For further in depth-analysis evaluations, the standard deviations of the calibration process and the image acquisition process, $u_{\mathrm{p,\,cal}}$ and $u_{\mathrm{p,img}}$, are used.

3. Experimental results of a DoE to assess the optical configuration

The DoE presented in the previous section was conducted using the modular SL scanner, the tactile CMM and the convertible test specimen in different configurations.

3.1. Results for flat test specimen configuration

The first four experiments of the DoE were conducted using the flat test specimen configuration. First, the results for the different features are presented in this section. Second, the effect of repeating the experiments is investigated in more detail. During this detailed analysis, the influence from repeating the calibration process is separated from the influence of repeating the image acquisition process.

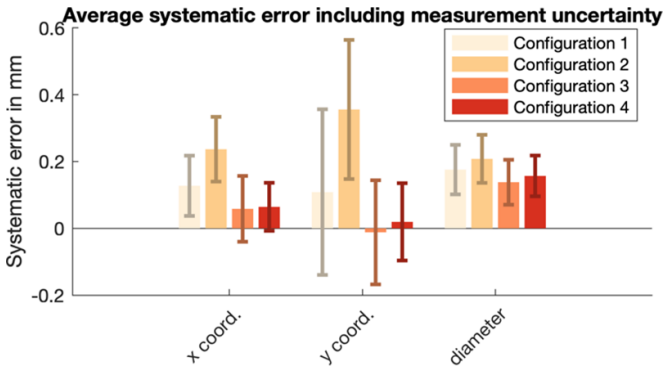

Figure 13. Systematic error and expanded measurement uncertainty for features x coordinate, y coordinate and diameter of the flat configuration of the test specimen.

3.1.1. Accuracy of measurements of the flat test specimen configuration. Figure 13 shows systematic errors b and the measurement uncertainty U for the x and y coordinates as well as the diameters of the flat configuration of the test specimen. Each optical configuration is represented by a bar with different color. The bars display the mean systematic error of all measurement features. They are calculated by determining the systematic error for each feature individually. Afterwards, the mean value is calculated for all features of the respective configuration. The error bars represent the mean uncertainty. As with the systematic error, they are calculated independently for each feature and then the mean value is calculated. Each bar contains all image repetitions and calibration repetitions. Thus, 5 calibration repetitions $\times$ 5 image acquisitions $\times$ 12 elements on the base plate $\times$ 4 holes per element on the base plate $=$ 1200 measurement values are included in each bar.

For all features, configurations 3 and 4 have the lowest systematic errors. For the x and y coordinates, the systematic measurement errors are less than 0.1 mm; for the diameter, they are less than 0.2 mm. Expanded measurement uncertainty is lower, as well. It follows that a long focal length (configurations 3 and 4) gives better results for the considered features. The influence of the baseline distance plays a minor role compared to the long focal length. However, with a short focal length, a narrow camera distance should be chosen to keep the errors low. Configuration 2 (large baseline distance and short focal length) leads to significantly worse results compared to configuration 1.

Perspective distortions are the reason for this behavior. They lead to holes appearing elliptical in images. The larger a hole is, the more significant this error becomes. As a result, the center of large holes on the base surface of the test specimen, which are used for registration, cannot be exactly detected.

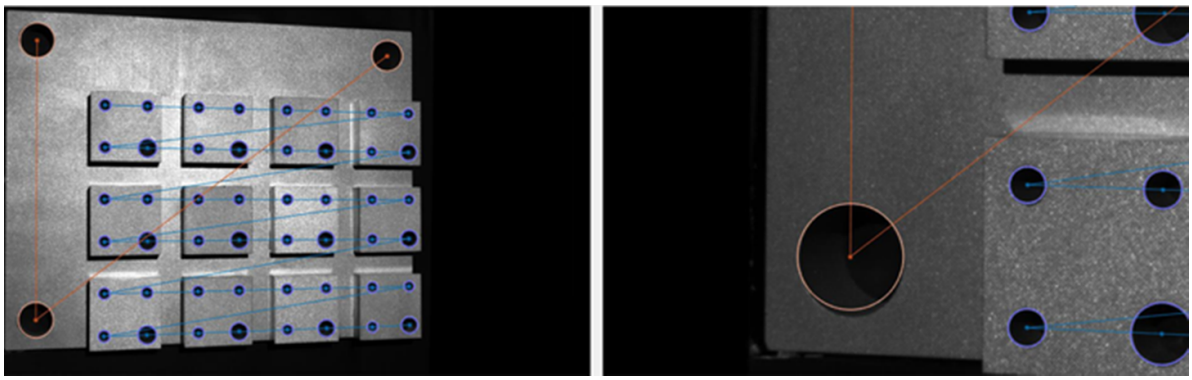

Figure 14. Perspective distortion using the example: flat specimen configuration, optical configuration.

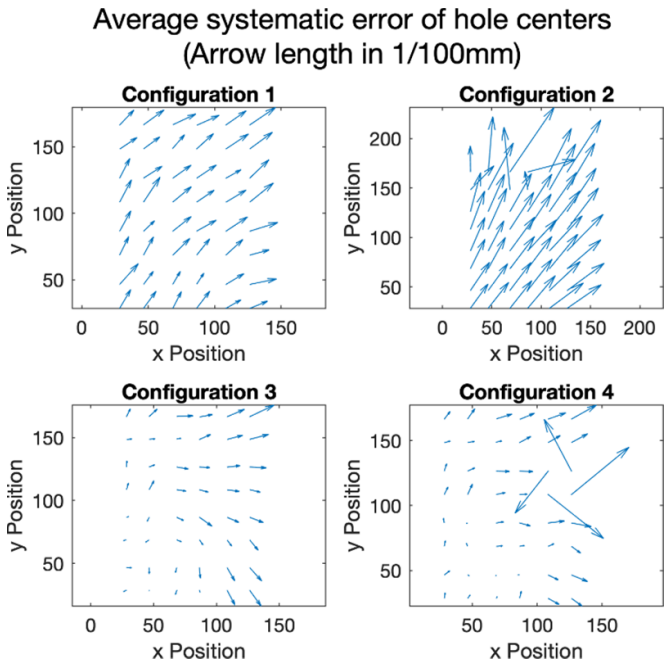

Figure 15. Effect of the perspective distortions of the optical configurations for the flat test specimen configuration.

Figure 14 shows this behavior as an example for optical configuration 2. It is visible that the hole is distorted in the image and that, therefore, the circle fitted to the hole's edge does not fit the hole's shape.

The effect of the perspective distortions is shown in figure 15 in the form of vector plots for all configurations of the flat test component configuration. The arrows indicate the systematic error of the hole x- and y-positions of the hole centers. Configurations 3 and 4 (long focal length) show the smallest systematic errors. This finding corresponds with the results above: Long focal lengths lead to low perspective distortions and, when using long focal lengths, the baseline distance has little influence. Figure 15 also highlights that configuration 2 leads to the largest systematic errors. This means that a short focal length in combination with a large baseline distance produces significant distortions of the image.

3.1.2. Comparison of the effect of repeating the calibrations process vs. repeating the image acquisition process for the flat test specimen configuration. The influence of repeating the calibration process and repeating the image acquisition process on the measurement results' standard deviation is investigated next. Up to now, each repetition of the image acquisition process was evaluated with each repetition of the calibration process to calculate the standard uncertainty of the measurement process u_p, giving a total of 25 evaluations for each experiment (compare section 2.3.2). For the following investigation, however, the repetitions of the calibration process and the image acquisition process are evaluated separately by calculating the standard deviations of the calibration process $u_{\mathrm{p,cal}}$ and of the image acquisition process $u_{\mathrm{p,img}}$ according to section 2.3.2. Evaluating these two parts of the measurement process independently from each other allows to deduct their respective influence on the measurement uncertainty, which may be caused by image noise or changes to the camera positions in-between repetitions of the calibration or image acquisition process.

First, the standard deviations of the calibration process' $u_{\mathrm{p,cal}}$ and of the image acquisition process' $u_{\mathrm{p,img}}$ were calculated for all control features' x coordinate, y coordinate and diameter of every configuration. Second, the mean values of the calibration process' and the image acquisition process' standard deviations of the x coordinates, the y coordinates and the diameters were determined for each configuration separately.

The mean values of the standard deviations of the calibration process and the measurement process are displayed in figure 16. The figure highlights that the y coordinates are strongly affected by repeating the calibration and image acquisition processes, while the diameters are least affected. Figure 16 further reveals that configuration 4 leads to the smallest standard deviations, while the other configurations behave differently for repeating the calibration process and the image acquisition process, as well as for the different types of features. Finally, the figure shows that the standard deviation of the image acquisition process is bigger than the standard deviation of the calibration process for all configurations and all types of measurement features (only exception being the x coordinate of configuration 3).

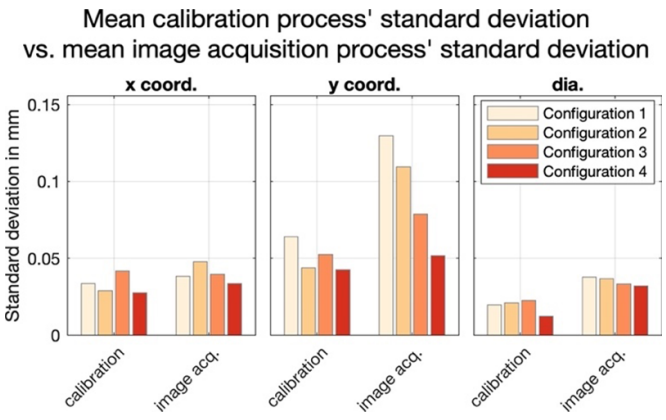

Figure 16. Mean values of the standard deviations of the calibration process and the measurement process of the x coordinates, the y coordinates and the diameters.

These findings allow to draw two conclusions. First, perspective distortions affect the measurement uncertainty in a similar but less pronounced way compared to the systematic errors of the previous subsection. Only a combination of a long focal length and a large baseline distance allows to significantly reduce measurement uncertainty. Second, repeating the image acquisition process has a stronger effect on the measurement uncertainty than repeating the calibration process. This applies to all types of measurement features and all optical configurations.

3.2. *Results for topographic test specimen configuration*

As before for the flat test specimen configuration, the accuracy of the measurements is first analyzed for the topographic test specimen configuration. Afterwards, the effect of repeating the calibration process and the image acquisition process on the measurements' standard deviation is investigated. For reference, table 3 provides a summary of the topographic test specimen's control features.

3.2.1. Accuracy of measurements of the topographic test specimen configuration. Figure 17 shows the x y, z coordinates' and diameters' results for the topographic test specimen configuration. This figure equals the results from figure 13, but now also includes the deviations in the z-direction.

These results confirm that a long focal length (configuration 3 and 4) is particularly well suited for the x coordinates, y coordinates and diameters. However, it shows that a small baseline distance combined with a short focal length (configuration 1) can lead to similarly good results for these features with the topographic test specimen configuration. All configurations show equally good results for the z coordinate.

Figures 18 and 19 show the results for the convex and concave elements, respectively. The results highlight that the systematic errors and the measurement uncertainty are correlated with the diameters. In case of large diameters, only a small part of the circumference of the measurement features is represented by triangulated points. This leads to small deviations

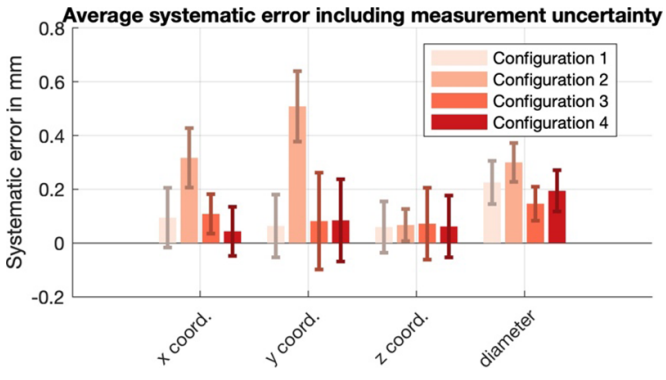

Figure 17. Systematic error and expanded measurement uncertainty of x, y, z coordinates and diameter of flat elements.

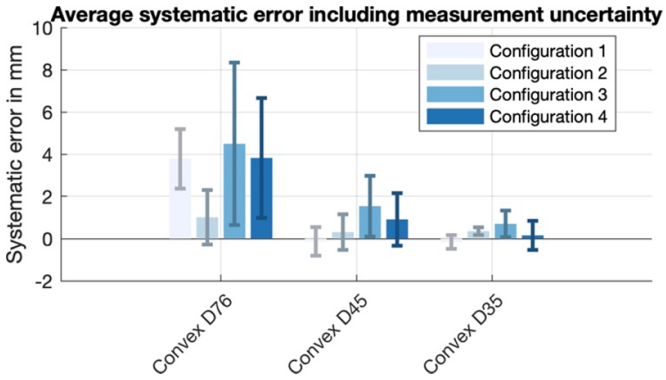

Figure 18. Systematic error and expanded measurement uncertainty for convex geometric elements.

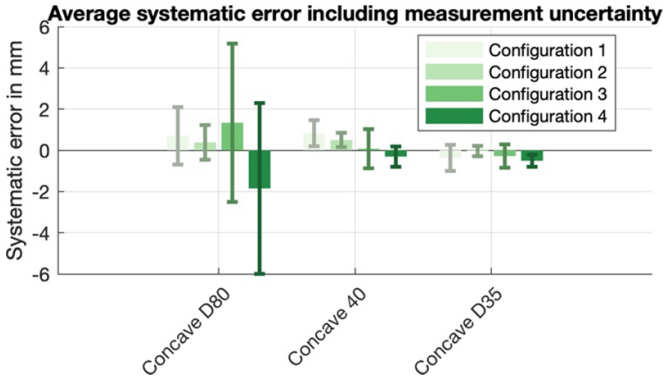

Figure 19. Systematic error and expanded measurement uncertainty for concave geometric elements.

having a large effect. Further, long focal lengths cause bigger systematic errors and bigger measurement uncertainties in case of some features (convex D76 and D45 as well as concave D80). As the measurement uncertainty is large compared to the systematic errors in these cases, more measurement repetitions could be necessary to ensure that the systematic errors were determined accurately.

Figure 20 displays the systematic errors and measurement uncertainties of the slanted planes. For configurations 1, 3 and 4, the slant angle has a minor effect on the systematic errors and the measurement uncertainties. Only configuration

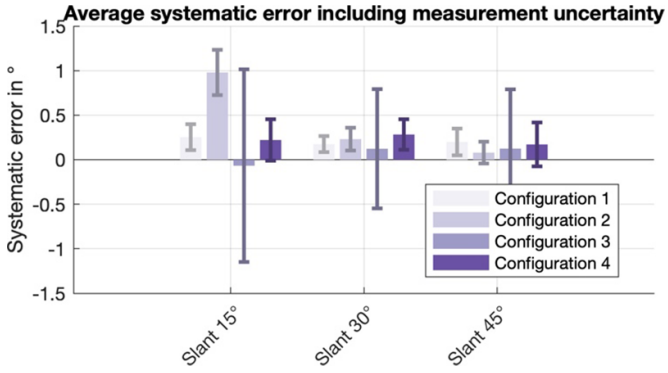

Figure 20. Systematic error and expanded measurement uncertainty for slanted planes.

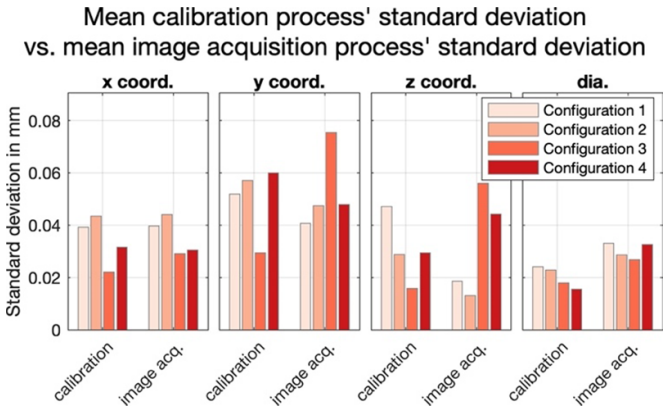

Figure 21. Mean standard deviations of the calibration process and the measurement process of features of type x coordinate, y coordinate, z coordinate and diameter.

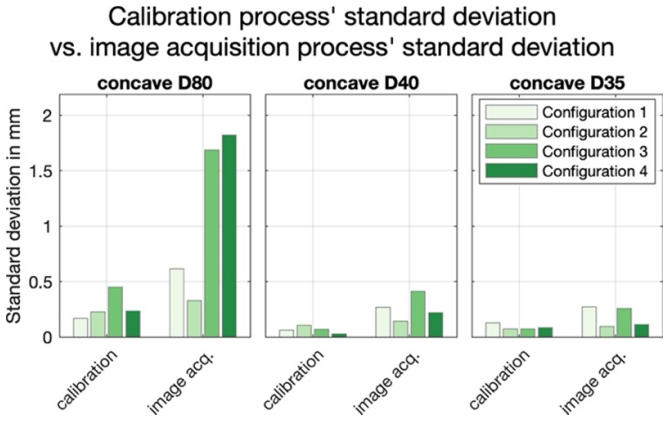

Figure 22. Standard deviations of the calibration process and the measurement process for concave geometric elements.

2 shows a large systematic error and uncertainty for slant 15°. This configuration is characterized by a large baseline and short focal lengths. As described above for the flat configuration of the test specimen, this configuration therefore promotes perspective distortions. Perspective distortions in combination with the shallow descend of slant 15° seems to lead to large systematic errors. Further, configuration 3 leads to large measurement uncertainty values for all slants. A detailed analysis on why this optical configuration causes large measurement uncertainties will be given in the next subsection.

Taking all geometric elements into account, the combination of a long focal length and large baseline distance (configuration 4) is favorable to achieve low systematic errors for the topographic test specimen configuration. Configuration 4 gives the best results for x, y and z coordinates of the flat planes. For the diameters and the other geometric elements, configuration 4 leads to systematic errors that are not clearly distinguishable from the best results due to the measurement uncertainty. However, it must be noted that configurations with a short camera distance (configurations 1 and 2) perform well for elements whose control feature values are directly calculated from the measurement feature values (concave, convex and slant). These features' control values are independent of the registration process, which can be influenced by perspective distortions, as demonstrated by figure 14. These features' systematic errors are nevertheless of a larger magnitude than those of the flats' x, y, z coordinates and diameters.

3.2.2. Comparison of the effect of repeating the calibrations process vs. repeating the image acquisition process for the topographic test specimen configuration. Figure 21 displays the mean values of the calibration process' and image acquisition process' standard deviations for the flat planes' features x, y, z coordinate and diameters. This figure resembles figure 16 of the flat test specimen configuration. However, for the topographical configuration, repeating the imaging process does not lead to distinctly larger standard deviations than repeating the calibration process. While the measurement results of the y coordinate are most affected by repeating the calibration and image acquisition process, it is impossible to establish a clear correspondence between type of control feature, type of repeated process and optical configuration or magnitude of standard deviation. It is noteworthy, though, that the image acquisitions' standard deviations of configurations with a short focal length (1 and 2) are lower for y coordinates when measuring the topographic configuration than they are for measuring the flat configuration (figure 16). This could be interpreted as the perspective distortions and the z position of the flats positively interfering.

Figures 22 and 23 depict the calibration process' and image acquisition process' standard deviations for convex and concave geometric elements, respectively. In contrast to the previously discussed figures of the flat elements, these figures show values for each element individually. In the figure, it is visible that the image acquisition process' standard deviation is bigger than the calibration process' standard deviation for concave and convex elements, except for one exception (convex D80 for configuration 2). Especially for convex elements, optical configurations 3 and 4, who both share a long focal length, lead to higher values of the image acquisition process' standard deviation compared to configurations with a short focal length.

Figure 24 shows the calibration process' and image acquisition process' standard deviations for the slanted planes. While

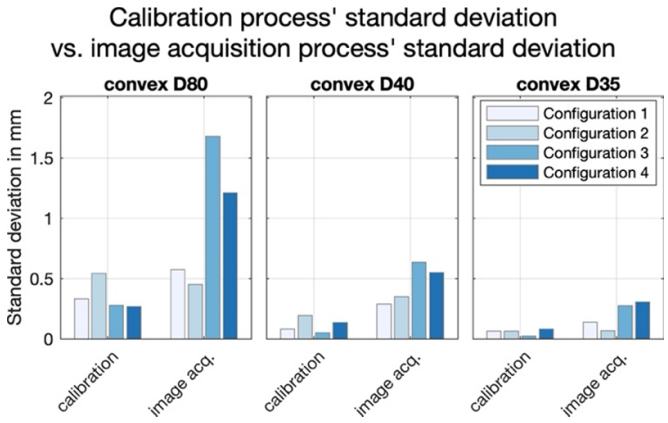

Figure 23. Standard deviations of the calibration process and the measurement process for convex geometric elements.

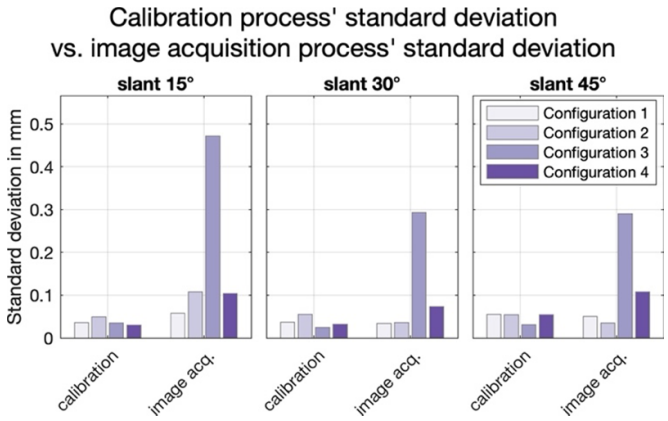

Figure 24. Standard deviations of the calibration process and the measurement process for slanted planes.

it is impossible to establish a clear relationship between type of standard deviation, optical configuration and feature for optical configurations 1 and 2, optical configurations 3 and 4 lead to the image acquisition process' standard deviation being larger than the calibration process' standard deviation. Especially optical configuration 3 promotes large values of the image acquisition process' standard deviation. This optical configuration features a small baseline distance and a long focal length. This leads to a small opening angle between the cameras, which could cause small movements of the topographic test specimen relative to the camera during measurement repetitions to have a large influence on the measurement results. This effect could be caused by the slanted angles of the control features interacting with the triangulation step of the image acquisition process.

Summarizing the findings regarding the calibration process' and imaging process' standard deviations, different trends are visible when measuring the topographical specimen configuration. As it is the case with systematic errors, the standard deviations of the flats' *x, y, z* coordinate and diameters are of the lowest magnitude. For convex and concave elements, the repetition of the image acquisition process has a more pronounced effect on the measurement results than repeating the calibration process. For slanted planes, this only applies to those optical configurations with long focal lengths. Further, long focal lengths do not help to achieve low standard deviations, in general, although configuration 4 with a long focal length led to the lowest systematic errors.

3.3. Conclusions from the results

The results show that the optical configuration and the geometric configuration of the test specimen have a pronounced effect on the measurement accuracy. This leads to the conclusion that the configuration of a SL scanner should be based on the specimen's shapes and the expected measurement features.

In general, the presented modular SL scanner and image processing process leads to accurate measurement results. Holes' center coordinates and distances can be measured with systematic errors of less than 0.1 mm. Geometrically more challenging elements, like the presented convex and concave elements, lead to bigger systematic errors, though.

In case of the test specimen's flat configuration, the holes' round shape is warped to an elliptical shape during the imaging process due to perspective distortions. Limiting perspective distortions through the optical configuration limits the deformation of the holes in the images and therefore improves the accuracy of the triangulation process. For mainly flat specimens, an optical configuration with long focal lengths and even a small baseline distance is therefore favorable. Such a configuration minimizes optical distortions and thus reduces measurement errors. While a configuration with a small baseline distance and long focal length allows tight packaging of a SL scanner, a long working distance is needed, though.

It is more difficult to identify an optimal optical configuration for topographical specimens, i.e. specimens with three dimensional features. For these, a long focal length in combination with a large baseline distance (configuration 4) leads to low systematic errors. However, configurations with a short focal length perform well for control features whose calculation is independent from the registration process, like the diameter of a concave surface. For these features, configurations with a short focal length lead to low systematic errors. Further, these configurations also limit the image acquisition process' contribution to the measurement uncertainty. While perspective distortions caused by shorter focal lengths have a distinct influence on circular measurement features, perspective distortions seem to have less of an impact on the triangulation of the points from the decoded line pattern. This leads to the conclusion, that configurations with a shorter focal length can deliver high accuracy when measuring topographical specimens. This note is especially important as these configurations only require a short working distance and are therefore beneficial to applications with limited space availability.

4. Discussion and outlook

To assess the influence of the optical configuration of a SL scanner on the measurement results, a modular SL scanner and

a convertible test specimen to simulate different geometries have been used. Systematically varying the optical configuration of the SL scanner and the configuration of the test specimen in a DoE showed that the optical configuration of the SL scanner has a pronounced effect on the measurement results. However, there is not one optical configuration that clearly leads to the most accurate results with all types of geometric elements and control features. In many cases, it is favorable to choose longer focal lengths and larger baseline distances. However, such configurations lead to a longer working distance and a need for more space for the sensor. Both may be undesirable in many applications. In general, more advanced image processing algorithms could be used to compensate for a sub-optimal optical configuration. However, this makes a SL scanner lesser flexible as it cannot be used on any given specimen. In conclusion, this work shows that a SL scanner's optical configuration needs to be tailored towards its anticipated use. The presented, convertible test specimen can be used for such a task-specific development. By using a configuration that resembles the expected specimens, a SL scanner's optimal optical configuration can be identified.

To evaluate the accuracy of the different optical configurations, tactile reference measurements of the convertible test specimen were carried out. Deploying an evaluation procedure based on DIN EN ISO 15530-3, it was possible to successfully differentiate between systematic errors and random errors. While DIN EN ISO 15530-3 demands for similar measurement techniques to be used, experience from the field of industrial CT shows that tactile reference measurements have already been successfully applied to image processing based measurement techniques [28]. Designing the measurement process of the SL scanner to closely resemble the tactile measurement process allowed to compare the measurement results from these different measurement technologies and was key to deploy this accuracy assessment method.

Analyzing the systematic errors shows that the optical configuration and the specimens' shape have a pronounced effect on the measurement accuracy. Further, repeating the whole measurement process, i.e. the image acquisition process and the calibration process, highlighted the benefits of a standardized calibration process. However, after establishing such a routine, the biggest influence on the measurement uncertainty stems from repeating the image acquisition process.

In summary, the presented work underlines the importance of the optical configuration of a SL scanner. Further, this work shows the importance of a procedure to evaluate not only random but also systematic errors when assessing a SL scanner's accuracy. Without tactile reference measurements, it would have been impossible to show the pronounced effect of systematic errors on the accuracy of a SL scanner. Although the same cameras and projector were used for all experiments, substantially different accuracies were achieved for different optical configurations.

In future experiments, it should be investigated whether the resolution of the SL scanner has an equally strong effect on the measurement accuracy as the optical configuration. High resolution camera sensors and different projection patterns may be deployed for such investigation. Additionally, a SL scanner only consisting of a projector and a single camera should be investigated, as well. Such configurations are typical for industrial applications because they only demand for one camera and thus save costs. However, such configurations may lead to a different behavior regarding the influence of the optical configuration on the measurement accuracy.

5. Summary

This paper deals with the accuracy of optical systems with structured light projection for 3D acquisition (SL scanners). From an analysis of the state of the art it has been deducted that the optical configuration of such a SL scanner has a pronounced influence on the accuracy. Therefore, the optical configuration has been investigated by deploying a modular SL scanner, whose cameras' focal lengths and baseline distance can be varied. To cover different measurement features and shapes of industrial specimens, a convertible test specimen was used. Additionally, based on the procedure described in DIN EN ISO 15530-3, reference measurements were carried out with tactile CMM to differentiate between systematic and random measurement errors. By closely modelling the SL scanner's measurement process after the CMM's, it has been shown that for many use-cases a long focal length and large baseline distance leads to improved accuracy. However, the type of measurement feature and thus the specimen's shape have a pronounced effect on the accuracy, as well.

Data availability statement

The data that support the findings of this study are openly available at the following URL/DOI: https://dx.doi.org/10.35097/543.

Acknowledgments

This work contributes to the research performed at KIT Karlsruhe Institute of Technology. It was funded by the BMBF funded project 'AgiloBat2' (03XP0369A) as part of the Cluster InZePro.

ORCID iDs

Leonard Schild https://orcid.org/0000-0001-5656-8779
Fabian Sasse https://orcid.org/0000-0002-8613-7301

References

[1] Giancola S, Valenti M and Sala R 2018 *A Survey on 3D Cameras: Metrological Comparison of Time-of-Flight, Structured-Light and Active Stereoscopy Technologies* (Cham: Springer) (https://doi.org/10.1007/978-3-319-91761-0)
[2] Van der Jeught S and Dirckx J J 2016 Real-time structured light profilometry: a review *Opt. Lasers Eng.* **87** 18–31
[3] Geng J 2011 Structured-light 3D surface imaging: a tutorial *Adv. Opt. Photonics* **3** 128–60

[4] Rachakonda P, Muralikrishnan B and Sawyer D Sources of errors in structured light 3D scanners *Dimensional Optical Metrology and Inspection for Practical Applications VIII*, (*Baltimore, United States*, *April 2019*) p 5 (available at: https://www.spiedigitallibrary.org/conference-proceedings-of-spie/10991/2518126/Sources-of-errors-in-structured-light-3D-scanners/10.1117/12.2518126.full)

[5] Sims-Waterhouse D, Isa M, Piano S and Leach R 2020 Uncertainty model for a traceable stereo-photogrammetry system *Precis. Eng.* **63** 1–9

[6] Wu F, Zhang Y, Ma X, Li X and Fan B (eds) 2019 *9th Int. Symp. on Advanced Optical Manufacturing and Testing Technologies: Optical Test, Measurement Technology, and Equipment* (SPIE)

[7] Liu J and Li Y 2014 Performance analysis of 3D shape measurement algorithm with a short baseline projector-camera system *Robot. Biomim.* **1** 1

[8] Sophian A, Sediono W, Salahudin M R, Shamsuli M S M and Zaaba D Q A A 2017 Evaluation of 3D-distance measurement accuracy of stereo-vision systems *Int. J. Appl. Eng. Res.* **12** 5946–51

[9] Setyawan R A, Soenoko R, Mudjirahardjo P and Choiron M A *Measurement Accuracy Analysis of Distance Between Cameras in Stereo Vision* pp 169–72

[10] Chen X, Xi J, Jin Y and Sun J 2009 Accurate calibration for a camera–projector measurement system based on structured light projection *Opt. Lasers Eng.* **47** 310–9

[11] Bräuer-Burchardt C, Ölsner S, Kühmstedt P and Notni G 2017 Comparison of calibration strategies for optical 3D scanners based on structured light projection using a new evaluation methodology *Videometrics, Range Imaging, and Applications XIV* (*Munich*, *26 July 2017*) vol 10332 pp 94–103

[12] Guerra M G, Lavecchia F and Galantucci L M 2020 Artefacts used for testing 3D optical-based scanners *Proc. 5th Int. Conf. on the Industry 4.0 Model for Advanced Manufacturing* (*Cham*) pp 173–89

[13] Li B and Song Z 2014 Structured light system calibration method with optimal fringe angle *Appl. Opt.* **53** 7942–50

[14] Li Z, Shi Y, Wang C and Wang Y 2008 Accurate calibration method for a structured light system *Opt. Eng.* **47** 053604

[15] An Y, Bell T, Li B, Xu J and Song Z 2016 Method for large-range structured light system calibration *Appl. Opt.* **55** 9563–72

[16] Zhang G and Wei Z 2002 A novel calibration approach to structured light 3D vision inspection *Opt. Laser Technol.* **34** 373–80

[17] Salvi J, Pagès J and Batlle J 2004 Pattern codification strategies in structured light systems *Pattern Recognit.* **37** 827–49

[18] Gupta M, Agrawal A, Veeraraghavan A and Narasimhan S G 2011 Structured light 3D scanning in the presence of global illumination *CVPR 2011* pp 713–20

[19] Li F, Stoddart D and Zwierzak I 2017 A performance test for a fringe projection scanner in various ambient light conditions *Proc. CIRP* **62** 400–4

[20] Eiríksson E R, Wilm J, Pedersen D and Aanæs H 2016 Precision and accuracy parameters in structured light 3D scanning *ISPRS—Int. Archives Photogrammetry, Remote Sensing and Spatial Information Sciences* pp 7–15

[21] Guerra M G, de Chiffre L, Lavecchia F and Galantucci L M 2020 Use of miniature step gauges to assess the performance of 3D optical scanners and to evaluate the accuracy of a novel additive manufacture process *Sensors* **20** 738

[22] Guerra M G, Gregersen S S, Frisvad J R, de Chiffre L, Lavecchia F and Galantucci L M 2020 Measurement of polymers with 3D optical scanners: evaluation of the subsurface scattering effect through five miniature step gauges *Meas. Sci. Technol.* **31** 15010

[23] Catalucci S, Senin N, Sims-Waterhouse D, Ziegelmeier S, Piano S and Leach R 2020 Measurement of complex freeform additively manufactured parts by structured light and photogrammetry *Measurement* **164** 108081

[24] Guidi G, Russo M, Magrassi G and Bordegoni M 2010 Performance evaluation of triangulation based range sensors *Sensors* **10** 7192–215

[25] Iuliano L, Minetola P and Salmi A 2010 Proposal of an innovative benchmark for comparison of the performance of contactless digitizers *Meas. Sci. Technol.* **21** 105102

[26] Ghandali P, Khameneifar F and Mayer J R R 2019 A pseudo-3D ball lattice artifact and method for evaluating the metrological performance of structured-light 3D scanners *Opt. Lasers Eng.* **121** 87–95

[27] Martínez-Pellitero S, Cuesta E, Giganto S and Barreiro J 2018 New procedure for qualification of structured light 3D scanners using an optical feature-based gauge *Opt. Lasers Eng.* **110** 193–206

[28] Müller P, Hiller J, Dai Y, Andreasen J L, Hansen H N and de Chiffre L 2014 Estimation of measurement uncertainties in x-ray computed tomography metrology using the substitution method *CIRP J. Manuf. Sci. Technol.* **7** 222–32

[29] Zhang S and Huang P 2006 Novel method for structured light system calibration *Opt. Eng.* **45**

[30] Heikkila J and Silven O 1997 A four-step camera calibration procedure with implicit image correction *Proc. IEEE Computer Society Conf. on Computer Vision and Pattern Recognition* (*San Juan, Puerto Rico*) pp 1106–12

[31] Steger C, Ulrich M and Wiedemann C (eds) 2018 *Machine Vision Algorithms and Applications* (Weinheim: Wiley-VCH) (available at: https://ebookcentral.proquest.com/lib/kxp/detail.action?docID=5131974)